metals

MDPI

Article

Thermal Hydraulics Analysis of the Distribution Zone in Small Modular Dual Fluid Reactor

Chunyu Liu [1,*], Xiaodong Li [1], Run Luo [1,2] and Rafael Macian-Juan [1]

[1] Chair of Nuclear Technology, Department of Mechanical Engineering, Technical University of Munich (TUM), Boltzmannstr. 15, 85748 Garching, Germany; xiaodong.li@tum.de (X.L.); run.luo@tum.de or luorun@usc.edu.cn (R.L.); rafael.macian@ntech.mw.tum.de (R.M.-J.)

[2] School of Resource & Environment and Safety Engineering, University of South China, No. 28, Changsheng West Road, Hengyang 421001, China

* Correspondence: chunyu.liu@tum.de or luoponan@gmail.com

Received: 29 June 2020; Accepted: 4 August 2020; Published: 6 August 2020

Abstract: The Small Modular Dual Fluid Reactor (SMDFR) is a novel molten salt reactor based on the dual fluid reactor concept, which employs molten salt as fuel and liquid lead/lead-bismuth eutectic (LBE) as coolant. A unique design of this reactor is the distribution zone, which locates under the core and joins the core region with the inlet pipes of molten salt and coolant. Since the distribution zone has a major influence on the heat removal capacity in the core region, the thermal hydraulics characteristics of the distribution zone have to be investigated. This paper focuses on the thermal hydraulics analysis of the distribution zone, which is conducted by the numerical simulation using COMSOL Multiphysics with the CFD (Computational Fluid Dynamics) module and the Heat Transfer module. The energy loss and heat exchange in the distribution zone are also quantitatively analyzed. The velocity and temperature distributions of both molten salt and coolant at the outlet of the distribution zone, as inlet of the core region, are produced. It can be observed that the outlet velocity profiles are proportional in magnitude to the inlet velocity ones with a similar shape. In addition, the results show that the heat transfer in the center region is enhanced due to the velocity distribution, which could compensate the power peak and flatten the temperature distribution for a higher power density.

Keywords: small module dual fluid reactor; molten salt reactor; CFD; thermal-hydraulics; heat removal by liquid metal

1. Introduction

1.1. The Small Modular Dual Fluid Reactor

The molten salt reactor is one of six Generation IV reactor types, which adopts molten salt as fuel and has many unique characteristics compared to solid fuel reactors. The study on two-fluid molten salt reactor can be traced back to 1966, when a two-fluid molten salt breeder reactor (MSBR) was designed at Oak Ridge National Laboratory (ORNL) [1]. The load-following capability of this MSBR system was studied for various ramp rates of the power demand [2]. Later a fast breeder reactor of about 2 GW thermal output using molten chlorides both as fuel and coolant was proposed [3].

A new design of the two-fluid MSBR called the Dual Fluid Reactor (DFR), which employs liquid lead instead of molten salt for the secondary circuit as coolant, was proposed by the researchers at the Institute for Solid-State Nuclear Physics (IFK) [4]. Differing from Taube's design, the high volumetric heat capacity of the liquid lead enables a significant heat removal capability and, thus, allows operation with a much higher power density than that of conventional reactors. A series of studies covering the neutronic characteristics, sensitivity performance, coupled calculations, emergency drain tank

estimation, depletion as well as hydraulic simulations can be found in references [5–10]. It has to be noticed that previous studies on the DFR focused mainly on a large type of reactor design with a thermal power of 3 GW. Yet, a smaller type of less than 0.3 GW would be more flexible and could be applied to a wider range of industrial processes, such as hydrogen production, water desalination, etc.

In this work a Small Modular Dual Fluid Reactor (SMDFR) is proposed with a nominal thermal power of 0.1 GW (100 MWt). The scheme is shown in Figure 1. The reactor core of the SMDFR, formed by hexagonally-arranged fuel tubes and surrounded by the reflector zone, is immersed at the center of a lead pool inside a cylindrical tank. As shown in Figure 2, the bottom and top of the core zone (from z = 0.2 m to z = 2.2 m) are joined by a distribution zone (from bottom, z = 0 m, to z = 0.2 m) and a collection zone (from z = 2.2 m to z = 2.4 m, symmetric with respect to the distribution zone), in order to distribute and collect the molten salt before and after flowing through the core region. Starting from the bottom part of the core region (Figure 2), the molten salt (depicted in golden color) goes into the distribution zone being distributed in the gaps between the hexagonally arranged coolant tubes (depicted in red) and then flows upwards inside the fuel tubes (depicted in golden color) through a plate with holes. After reaching the upper core part, it flows into the collection zone and then leaves the core region towards a chemical processing plant, which is employed for the online processing of the molten salt. During the operation, the salt coming from the collection zone is continuously passed to the chemical processing plant, in which the fission products are removed, and nuclear fuel components can be removed or added to maintain the optimal fuel composition. After being processed, it is pumped back into the bottom part for the next flow cycle through the core region. The liquid lead (Figure 2), acting as coolant in the secondary circuit, flows from the bottom center to the top center to cool down the core, which is heated by the nuclear fission reactions occurring in the molten salt. Upon leaving the core region, it is pumped to the heat exchanger located in the peripheral region of the tank and then transfers the heat to the tertiary circuit for utilization. Compared to the original design, the SMDFR is scaled down to 0.1 GW (100 MW), which makes it particularly suitable for providing energy for production facilities (e.g., water desalination [11], hydrogen production, or mines) in remote locations and more flexible, since it does not necessarily need to be hooked into a large power grid, and is able to be attached to other modules to provide increased power supplies if necessary. In addition, it also has changed from a pipe-type to a pool-type reactor in order to ensure the capability of establishing natural circulation during reactor transients or accidents. The hexagonal arrangement of fuel and coolant tubes realizes a dense lattice in the core and a high power density.

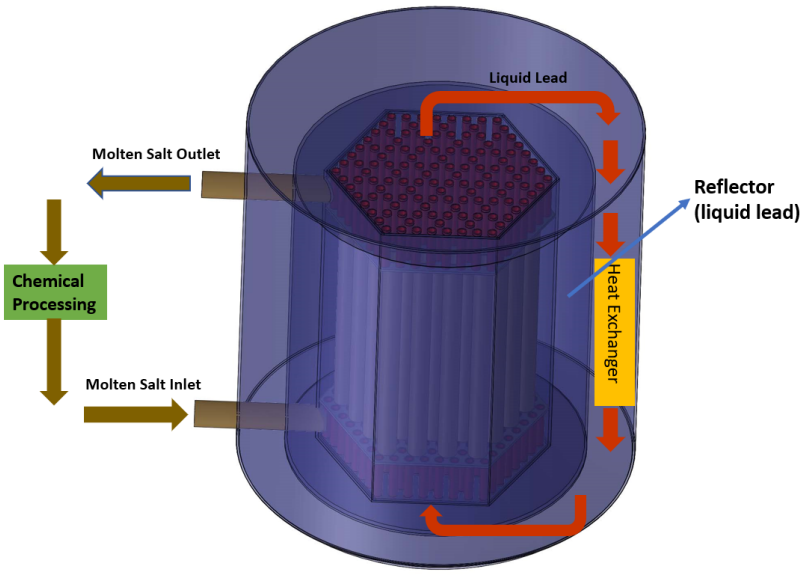

Figure 1. Design schematic of the Small Modular Dual Fluid Reactor.

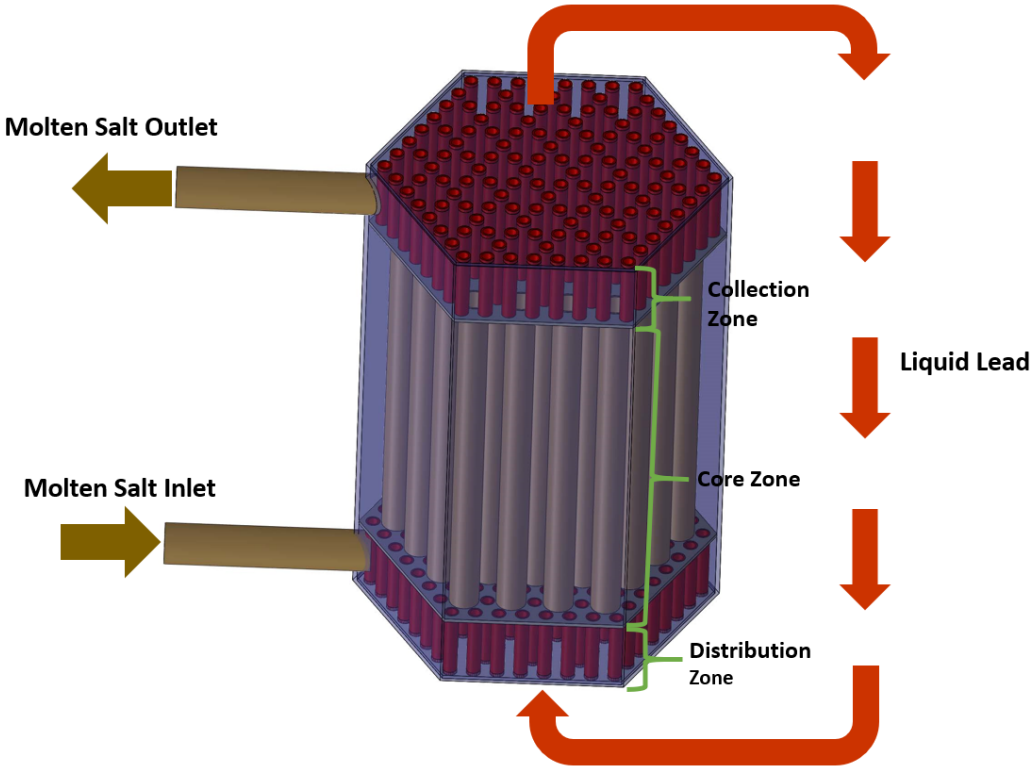

Figure 2. Schematic of the primary circuit (golden) and the secondary ciruit (red) of the Small Modular Dual Fluid Reactor.

The technical data of the SMDFR are listed in Table 1. In this work a mixture of uranium tetrachloride and plutonium tetrachloride is chosen as fuel salt and the liquid lead is chosen as coolant. For the pipe walls silicon carbide is employed. The thermo-physical properties of these materials are listed in Table 2 according to [12–15]. The formulas in the reference are applied for each 100 K interval from 800 K to 1600 K (below the boiling point of molten salt: 1950 K [15]), which includes the operational temperature range. The corresponding interpolated values based on these temperature points are applied for the calculations.

Table 1. SMDFR technical data.

Parameters	Values
Core zone D × H (m)	0.95 × 2.0
Distribution zone D × H (m)	0.95 × 0.2
Collection zone D × H (m)	0.95 × 0.2
Height of core (m)	2.4
Outer reflector diameter (m)	1.25
Tank D × H (m)	1.65 × 3.4
Number of fuel tubes	1027
Fuel pin pitch (m)	0.025
Outer/interior fuel tube diameter (m)	0.008/0.007
Outer/interior coolant tube diameter (m)	0.005/0.004
Mean linear power density (W/cm)	609
Fuel inlet/outlet temperature (K)	1300/1300
Coolant inlet/outlet temperature (K)	973/1250
Fuel inlet/in-core velocity (m/s)	3/0.5225
Coolant inlet/in-core velocity (m/s)	5/1.3488

Table 2. Thermophysical properties of the two fluids and wall material.

	Formula	Validity Range [K]
Fuel specific heat capacity C_p (g/cm^3)	400	[-]
Fuel thermal conductivity k (W/(m·K))	2	[-]
Fuel density ρ (kg/m^3)	$1000 \times (5.601 - 1.5222 \times 10^{-3} \times T)$	[-]
Fuel dynamic viscosity μ (Pa·s)	4.50×10^{-4}	[-]
Coolant specific heat capacity C_p (g/cm^3)	$176.2 - 0.04923 \times T + 1.544 \times 10^{-5} \times T^2 - 1.524 \times 10^6 * T^{-2}$	[600–1500]
Coolant thermal conductivity k (W/(m·K))	$9.2 + 0.011 \times T$	[600–1300]
Coolant density ρ (kg/m^3)	$11,441 - 1.2795 \times T$	[600–2000]
Coolant dynamic viscosity μ (Pa·s)	$4.55 \times 10^{-4} \times e^{1069/T}$	[600–1473]
Pipe wall heat capacity C_p (g/cm^3)	690	[-]
Pipe wall conductivity k (W/(m·K))	$61,100/(T - 115)$	[300–2300]
Pipe wall density ρ (kg/m^3)	3210	[-]

1.2. Simulation Code

COMSOL Multiphysics (version 5.5, COMSOL Inc., Stockholm, Sweden) [16] together with its CFD (Computational Fluid Dynamics) module [17] and Heat Transfer module [18] is used to perform the 3D pin-by-pin (for all tubes) thermal-hydraulics calculation. COMSOL Multiphysics is a multi-physics simulation code package which is used in many industry application, including fluid flow, and can provide a high accuracy numerical solution by using the Finite Element Method (FEM) to solve the corresponding set of partial differential equations. The software runs on a standalone PC with Intel® Core™ i7-7700 processor, 64 GB RAM and solid state disk.

1.3. Research Objective

A novel design of the core (including the distribution zone, core zone and collection zone) for a small modular dual fluid reactor is proposed and the thermal hydraulics characteristics of the distribution zone are investigated. In order to obtain both systematic and local behaviors of the two fluids, a 3D computer model is built using COMSOL Multiphysics with the CFD and Heat Transfer modules and the corresponding numerical simulations are performed. In addition, the sensitivity analysis is conducted to investigate the system responses of various inlet velocities of both fluids.

2. Modeling and Simulation

The modeling and simulation process presented in this paper is divided into four parts: geometry extraction and building, setup of governing equations, meshing, selection of the numerical solver and performing the simulation.

2.1. Geometry

There are many more fuel tubes than those depicted in Figure 3, and a full core calculation requires very large computational resources. Because of the symmetrical hexagonal configuration of the core region, a sector of 30° (Figure 4, right) of the lower part of the core with a height of 0.4 m (from z = 0 m to z = 0.4 m, Figure 4, left) around the central cylindrical axis, only one twelfth of the complete geometry, was selected to represent the full scale geometry by applying symmetric boundary conditions (mirror plane) [10]. The number of fuel tubes to be simulated was then decreased from 1027 to 100, among which 72 are complete tubes. A complete tube means that the whole tube was included in the selected 30° sector and an incomplete tube means only one part of the tube was included. The tubes at the boundary were incomplete tubes, as shown in Figure 4 (right).

In Figure 4 (right) three colored domains can be observed: golden, red and grey, which represent respectively the fuel domain, the coolant domain, and the pipe wall domain. This geometric model contained the distribution zone with a height of 0.2 m and its upper part (from core zone) with a

height of 0.2 m. In the fuel domain, the molten salt entered through the inlet pipe from the right side, flowed into the distribution zone, spread inside the gaps between the hexagonally-arranged coolant tubes, flowed upwards into the fuel tubes, and then left the core zone through the upper part. In the coolant domain, the liquid lead flowed into the core zone through the bottom coolant pipes, it then flowed upwards between the gaps along the fuel tubes, and, finally, it left the core region through the upper part.

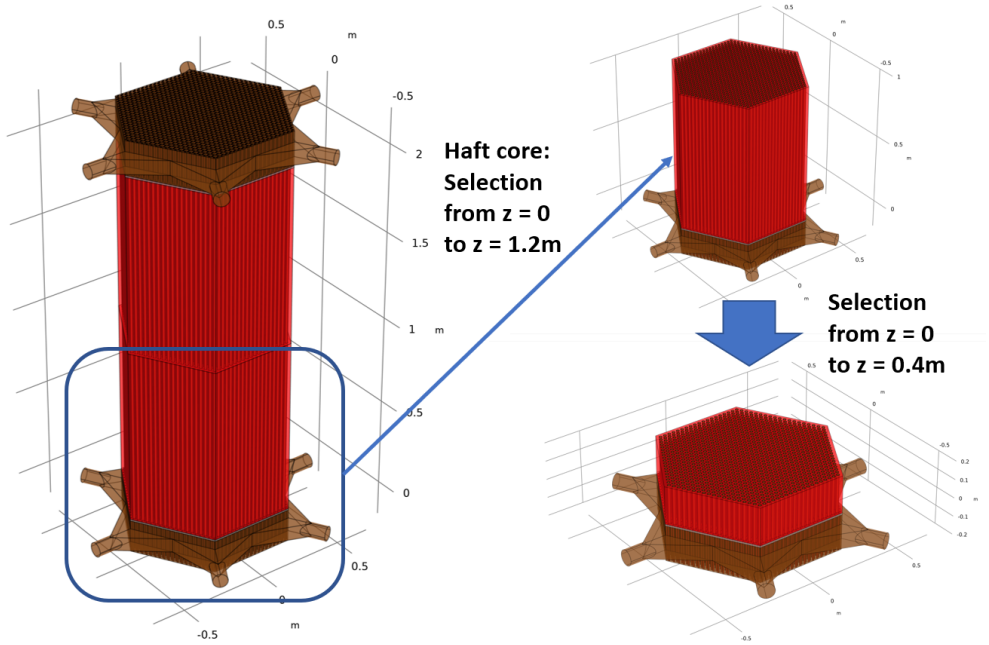

Figure 3. The arrangement of both fuel and coolant tubes in a real core: left, full height, z = 0 m to z = 2.4 m; upper right, half height, z = 0 m to z = 1.2 m; lower right, z = 0 m to z = 0.4 m.

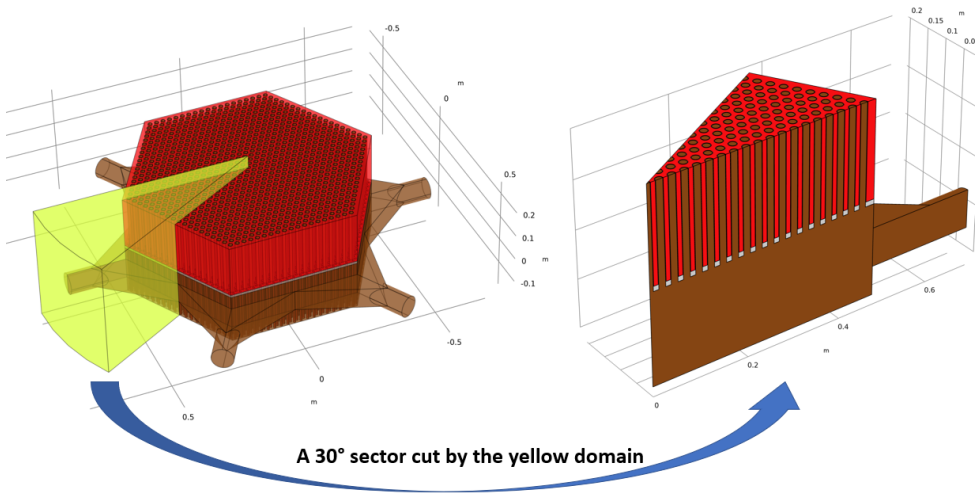

Figure 4. A 30° sector of the distribution zone and core zone with a height of 0.4 m, z = 0 m to z = 0.4 m.

2.2. Governing Equations

Heat transfer between two fluids separated by a solid wall was the main thermal process to be simulated, with both fluids the molten salt and the liquid lead having high Reynolds numbers (molten salt: 1.17×10^4, liquid lead: 1.28×10^4). Therefore, the physical COMSOL Multiphysics-interface "Conjugate Heat Transfer: Turbulent Flow, k-ϵ" is chosen for the calculation, which combines the "Heat

Transfer in Solids and Fluids" interface and the "Turbulent Flow, k-ϵ" interface and, thus, can be used to simulate the coupling between heat transfer and fluid flow.

Three compressibility options are available in COMSOL Multiphysics: compressible flow (Ma < 0.3), weakly compressible flow, and incompressible flow. The option of compressible flow makes no assumptions for the system and takes into account any dependency that the fluid properties may have on the variables. The equations of weakly compressible flow look the same as these of compressible flow except that the density is evaluated at the reference absolute pressure. For the incompressible flow option, the density is regarded as constant and evaluated using the reference temperature and pressure. [19] Since the density of molten salt has a strong dependency on its temperature, the weakly compressible Reynolds-Averaged Navier–Stokes (RANS) equations were adopted as a compromise between computational cost and accuracy:

$$\rho(\mathbf{u}\cdot\bigtriangledown)\mathbf{u} = \bigtriangledown\cdot[-p\mathbf{I}+\mathbf{K}]+\mathbf{F} \tag{1}$$

$$\bigtriangledown\cdot(\rho\mathbf{u}) = 0 \tag{2}$$

$$\mathbf{K} = (\mu+\mu_T)(\bigtriangledown\mathbf{u}+(\bigtriangledown\mathbf{u})^T)-\frac{2}{3}(\mu+\mu_T)(\bigtriangledown\cdot\mathbf{u})-\frac{2}{3}\rho k\mathbf{I} \tag{3}$$

where **K** is the viscosity term taking into account the interactions between the fluctuating parts of the velocity field. In order to close the above equations, two additional transport equations with two dependent variables, the turbulent kinetic energy k and the turbulent dissipation rate ϵ, are introduced:

$$\rho(\mathbf{u}\cdot\bigtriangledown)k = \bigtriangledown\cdot[(\mu+\frac{\mu_T}{\sigma_k})\bigtriangledown k]+P_k-\rho\epsilon \tag{4}$$

$$\rho(\mathbf{u}\cdot\bigtriangledown)\epsilon = \bigtriangledown\cdot[(\mu+\frac{\mu_T}{\sigma_\epsilon})\bigtriangledown \epsilon]+C_{\epsilon1}\frac{\epsilon}{k}P_k-C_{\epsilon2}\rho\frac{\epsilon^2}{k} \tag{5}$$

where μ_T and P_k are the turbulent viscosity and the production term and are given by:

$$\mu_t = \rho C_\mu\frac{k^2}{\epsilon} \tag{6}$$

$$P_k = \mu_T[\bigtriangledown\mathbf{u}:(\bigtriangledown\mathbf{u}+(\bigtriangledown\mathbf{u})^T)-\frac{2}{3}(\bigtriangledown\cdot\mathbf{u})^2]-\frac{2}{3}\rho k\bigtriangledown\cdot\mathbf{u} \tag{7}$$

The model's constants used are: $C_{\epsilon1}=1.44$, $C_{\epsilon2}=1.92$, $C_\mu=0.09$, $\sigma_k=1.0$, $\sigma_\epsilon=1.3$.

For the heat transfer in solids and fluids, the following equations are adopted:

$$\rho C_p\mathbf{u}\cdot\bigtriangledown T+\bigtriangledown\cdot\mathbf{q} = Q \tag{8}$$

$$\mathbf{q} = -k\bigtriangledown T \tag{9}$$

and the heat flux between the fluid with temperature T_f and the wall with temperature T_w is calculated by:

$$-\mathbf{n}\cdot\mathbf{q} = \rho C_p u_\tau\frac{T_w-T_f}{T^+} \tag{10}$$

Since there is no recommended turbulent Prandtl number model for liquid lead flow, the Kays–Crawford model is adopted:

$$Pr_T = \left\{\frac{1}{2Pr_T\infty}+\frac{0.3}{\sqrt{Pr_T\infty}}\frac{C_p\mu_T}{k}-(0.3\frac{C_p\mu_T}{k})^2(1-e^{-k/(0.3C_p\mu_T\sqrt{Pr_T\infty})})\right\}^{-1} \tag{11}$$

where the Prandtl number at infinity is $Pr_T\infty = 0.85$.

2.3. Meshing

The mesh was manually built by defining swept meshes and free tetrahedral meshes of various sizes for different regions. Since the flows of molten salt and liquid lead vary gradually along their channels, inside and outside the pipes, the finite elements can be quite stretched in the z-axial direction. For this reason, swept meshes were adopted in order to reduce the complexity of the mesh. The remaining parts of the model were relatively irregular and, thus, they were meshed by free tetrahedral mesh elements. The completely generated mesh (Figure 5) has 599,333 elements with an average element quality of 0.6259, and its 3D-plot of mesh element quality is shown in Figure 6. Around 96.9% of the model volume was filled by the mesh elements with qualities greater than 0.1, which is considered accurate enough [20]. From the numerical point of view such a mesh was acceptable in terms of accuracy and stability of the solution.

Six boundary layers were added for both the molten salt and the liquid lead with a stretching factor of 1.1. To achieve a high accuracy the value of the wall resolution in viscous units was set to lie between 11.6 and 100, which corresponded to 4.12×10^{-4} m for the molten salt and to 6.645×10^{-5} m for the liquid lead.

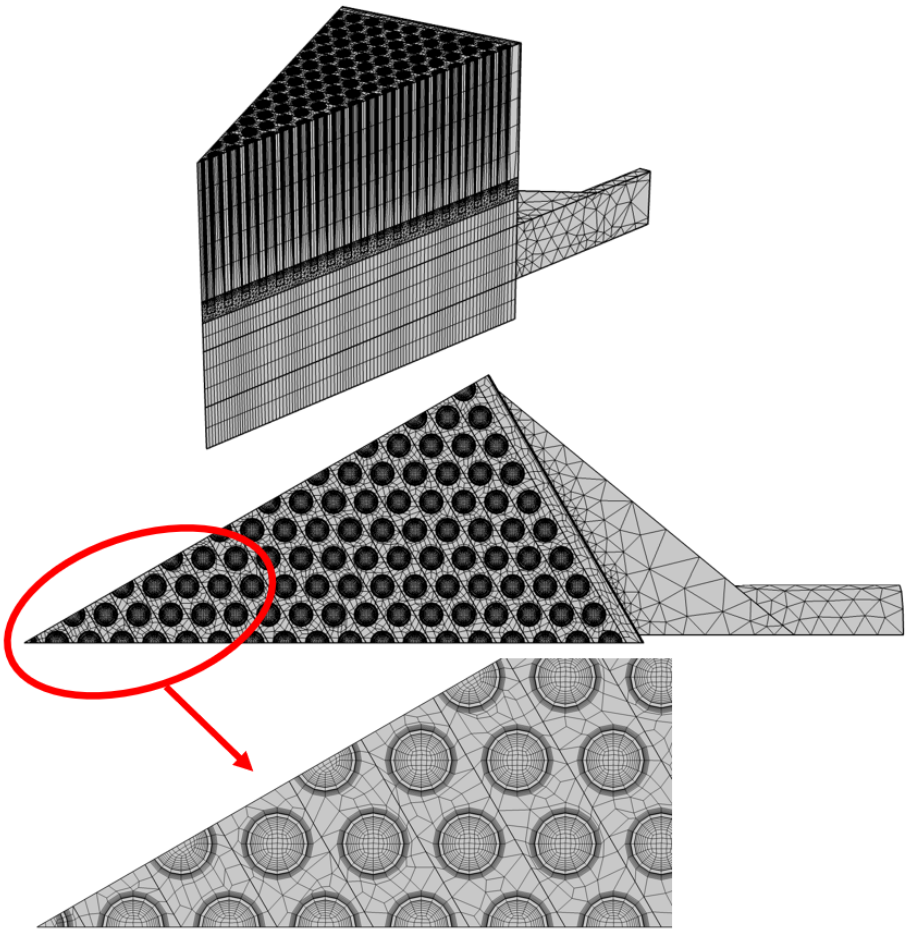

Figure 5. Model with mesh rendering: top, 3D view; middle, top view, xy-plane; bottom, top view zoomed up.

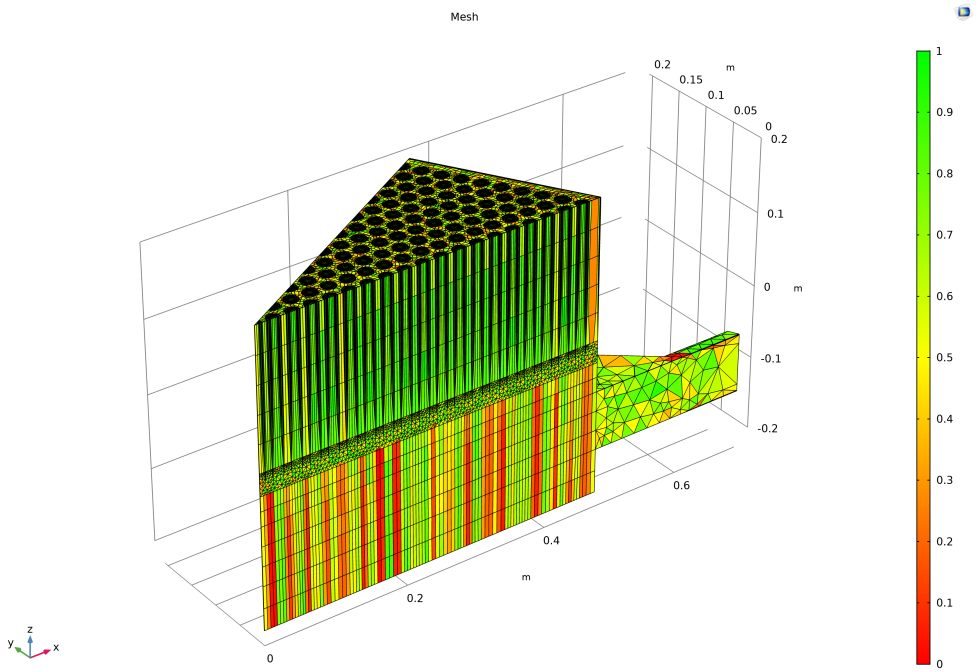

Figure 6. Mesh element quality with color indicating its value.

2.4. Numerical Solver

Two fundamental classes of solvers, direct and iterative solvers, were provided by COMSOL Multiphysics. The direct solvers available within COMSOL Multiphysics are "PARDISO", "MUMPS", and "SPOOLES", as well as "Dense Matrix" solvers. The Dense Matrix Solver can be only used for Boundary Element Method models, and therefore not suitable for the model in this paper. Contrary to direct solvers, iterative solvers approach the solution gradually and consume less memory, rather than in one large computational step. Three direct solvers, "PARDISO", "MUMPS", "SPOOLES", and one iterative solver, "GMRES", were selected for solving the same model, and the convergence criterion used for all variables was a relative tolerance of 0.005. Their performance comparison is listed in Table 3.

Table 3. Performance comparison of different solvers.

Solver	Solution Time [s]	Physical Memory [GB]	Virtual Memory [GB]
PARDISO	31,611	51.84	61.23
MUMPS	32,211	41.15	49.17
SPOOLES	103,898	56.43	57.41
GMRES	47,446	24.89	27.13

"PARDISO" was the fastest solver while consuming the highest physical and virtual memories except for "SPOOLES". The iterative solver "GMRES" consumed less memory and was slower then the direct solvers "PARDISO" and "MUMPS". All these solvers converged to the same results. Since the sizes of physical and virtual memories were not a bottleneck for the model to be solved, "PARDISO" was considered as the most efficient solver and was selected for solving all the simulations shown in this paper.

3. Results and Discussion

The results and discussion section is divided into four parts: verification, hydraulic characteristics, heat transfer analysis, and sensitivity analysis of inlet velocities.

3.1. Verification

Since the SMDFR design is a new concept and no experimental data can be used as a reference, the solution should be verified through the wall resolution in viscous units for the first layer, and also the consistence of results from different mesh scenarios for the mesh convergence.

The value of wall resolution in viscous units tells how far into the boundary layer the computational domain starts and should be lower than 500 to ensure that the logarithmic layer meets the viscous sublayer. As shown in Figure 7, for more than 90% of the fluid domains the value of the wall resolution in viscous units lay between 11.6 and 100, which means the first boundary layers approximately corresponded to the beginning of the logarithmic layer and the required accuracy of the results through the first boundary layers (next to the wall) was achieved. There was no need to further refine the boundary layer mesh.

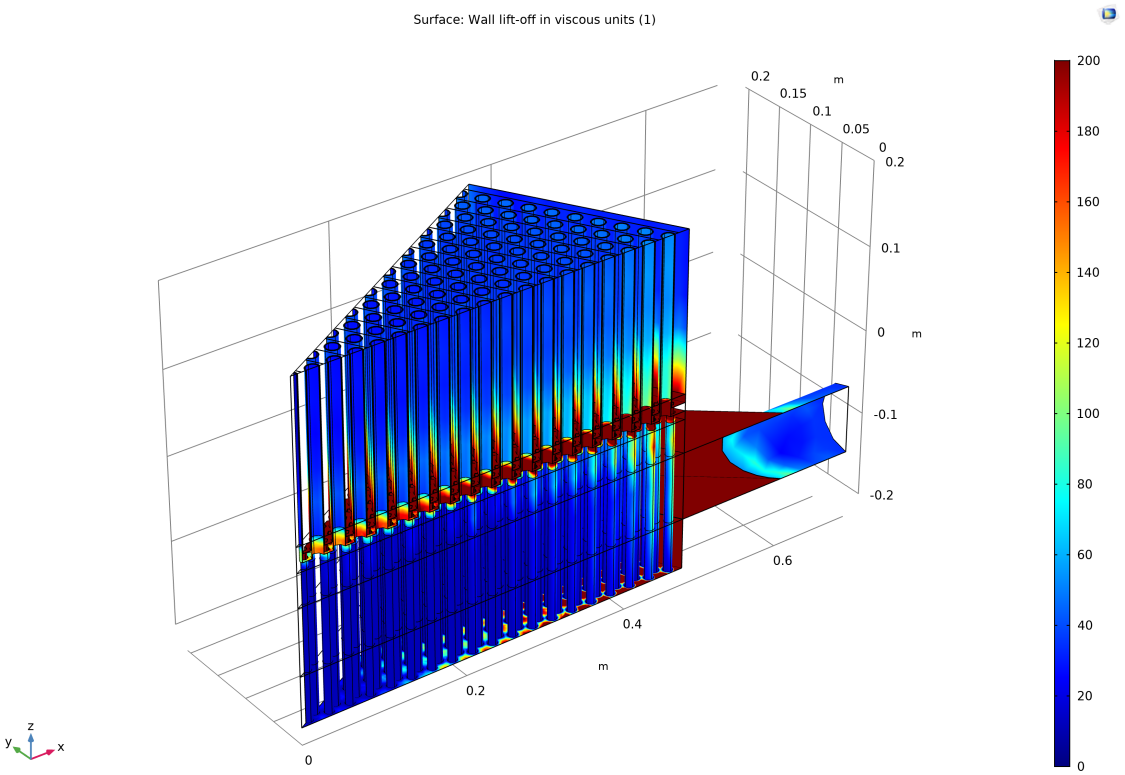

Figure 7. Wall lift-off in viscous units [1] at the wall surface.

In order to investigate the mesh convergence, five mesh scenarios (M0 to M4) were selected, M0 was the original mesh with six boundary layers, M1 and M2 had three and eight boundary layers respectively, and M3 and M4 have coarse and refined meshes separately. The meshing parameters are shown in Table 4. In order to quantify the simulation results for comparison and analysis, the outlet surface was divided into 19 channels for molten salt, and 20 channels for liquid lead, along the radial direction from center to circumference, as shown in Figure 8. The mass flow rate averaged velocity and temperature of each channel were selected as the quantities to be compared and analyzed.

As shown in Figures 9 and 10, all the mesh scenarios delivered consistent results for velocity and temperature profiles of both molten salt and liquid lead, especially in the peripheral regions. However, in the center regions (next to the center-line/axis of the core), some divergences were observed for M1 (black) and M3 (green). In order to ensure a high enough accuracy in the whole domain, M0 (red), which had consistent results with M2 (magenta) and M4 (blue) but consumed less computational resources, was verified against the finer meshes and adopted for the final simulations.

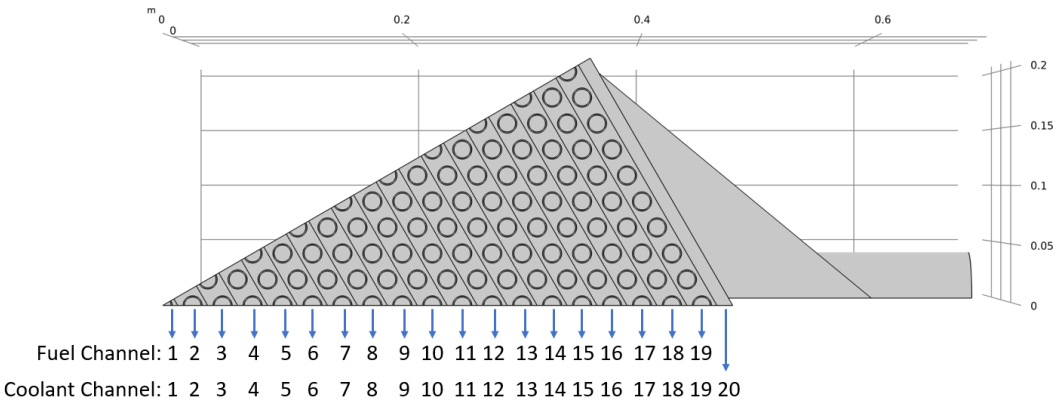

Figure 8. The channel indices of molten salt (fuel) and liquid lead (coolant) at the outlet plane.

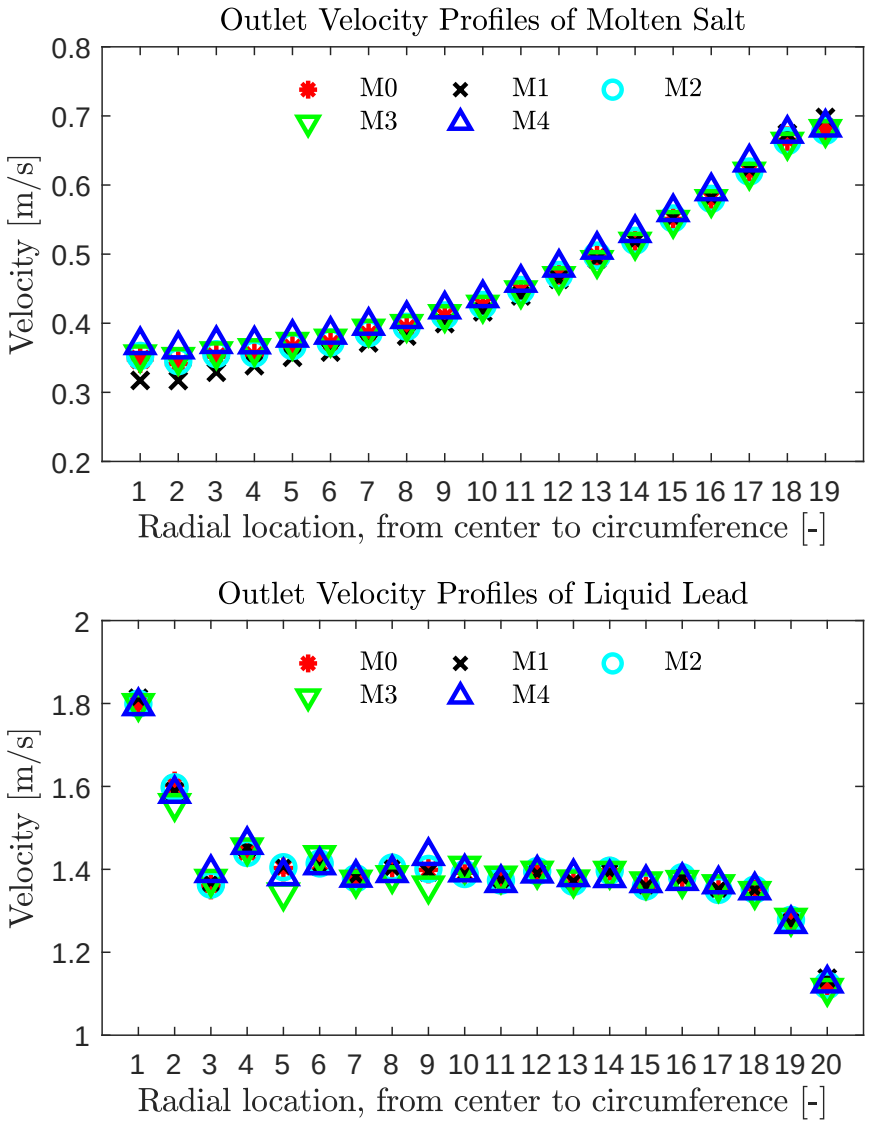

Figure 9. Mesh convergence study of outlet velocity distribution: top, velocity profiles of molten salt; bottom, velocity profiles of liquid lead.

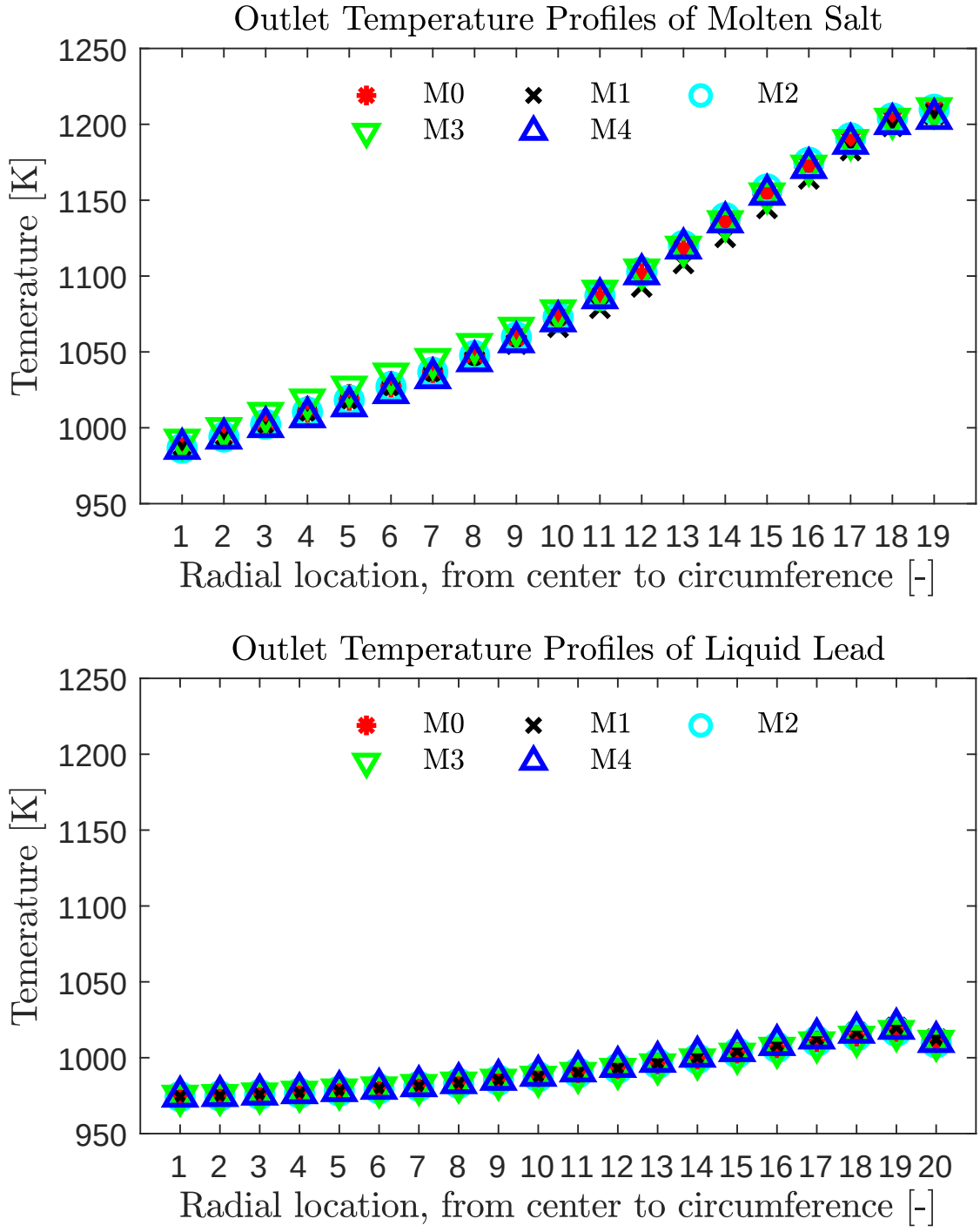

Figure 10. Mesh convergence study of outlet temperature distribution: top, temperature profiles of molten salt; bottom, temperature profiles of liquid lead.

3.2. Hydraulic Characteristics

From Figure 9 it can be seen that the molten salt velocity was relatively low in the central regions, which was caused by the high flowing resistance of the cross-flow through the coolant tubes. In order to get a better understanding of this phenomenon, a plane of the fuel inlet pipe was obtained by cutting the model by the blue plane (z = −0.1 m), as shown in Figure 11 (top). A majority of the molten salt tended to go upwards along the fuel tubes and only a small portion of the molten salt could pass the peripheral regions and reach the central core regions (Figure 11, bottom). Taking a look into the the

velocity vector field (Figure 12), one cold and two hot vortices could be observed located at the lower left corner (cold), top right corner (hot) and lower right corner (hot). Special consideration must be given to these locations, since the risk of structure material failure was relatively high and vibration might occur in the regions with vortices.

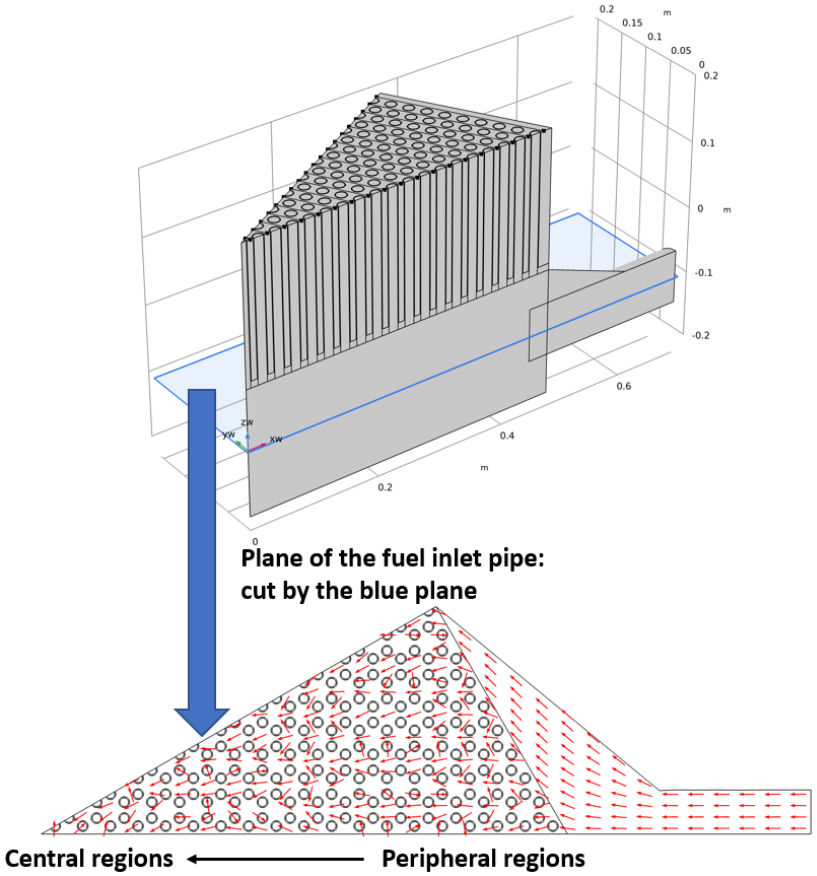

Figure 11. Top, plane of the fuel inlet pipe cut by the blue plane; bottom, Velocity vector field on the plane of the fuel inlet pipe of the molten salt.

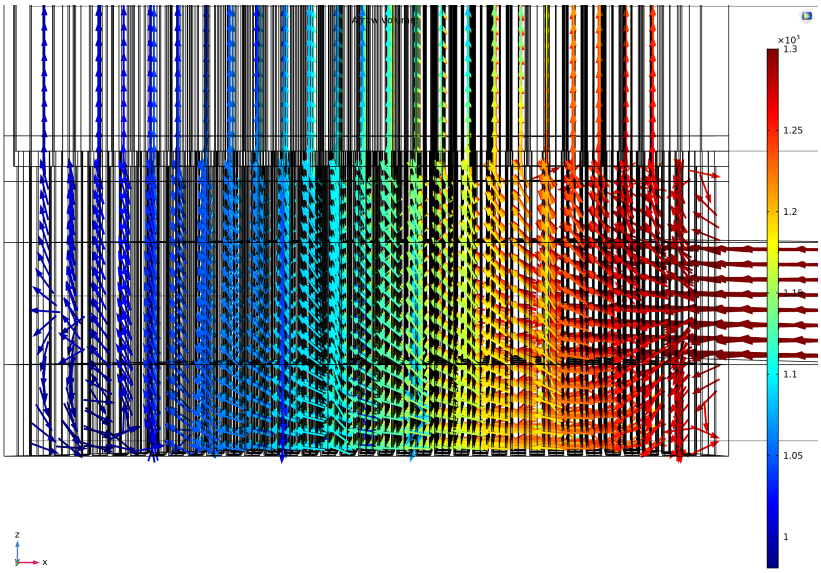

Figure 12. Velocity vector field of the molten salt with color indicating its temperature.

For liquid lead the situation was the contrary, starting from the first two channels it had a high velocity and after that the velocity became relatively uniform until the last two channels (Figure 9). Since in the region next to the circumference there was an additional channel surrounding the fuel channels, a certain portion of liquid lead was distributed to this channel and thus the velocity in peripheral region was reduced. However, the liquid lead in the central region (first two channels) accumulated due to the symmetry structure and thus had a relatively high velocity compared to others.

In order to quantify the energy loss during the flowing, Bernoulli's equation applied for a micro element of fluid is introduced:

$$\frac{P_1}{\rho_1 g} + z_1 + \frac{{u_1}^2}{2g} = \frac{P_2}{\rho_2 g} + z_2 + \frac{{u_2}^2}{2g} + {h_w}' \tag{12}$$

multiplying both sides by a micro flow element dm ($dm = \rho_1 g u_1 dA_1 = \rho_2 g u_2 dA_2$), and then integrating both sides by the corresponding cross section areas A_1 and A_2:

$$\int_{A_1} (P_1 + \rho_1 g z_1) u_1 dA_1 + \int_{A_1} \frac{1}{2} \rho_1 {u_1}^3 dA_1 = \int_{A_2} (P_2 + \rho_2 g z_2) u_2 dA_2 + \int_{A_2} \frac{1}{2} \rho_2 {u_2}^3 dA_2 + h_w \tag{13}$$

where h_w is the energy loss in W, which determines the demand of pumping power. Selecting the inlet and outlet cross section areas of the fluids as A_1 and A_2, the energy loss in the distribution zone was then obtained, which equals h_w. The h_w of molten salt in the distribution zone (for this one twelfth core sector) is 64 W, which was much lower if compared to that of the liquid lead. Since the heat removal function was mainly accomplished by the liquid lead, the flowing of molten salt is only needed for chemical processing and its mass flow rate does not have to be large. Due to its high mass flow rate the h_w of liquid lead (for this one twelfth sector) was quite significant: 14,515 W. Considering the whole structure and including the collection zone with the assumption of complete symmetry, the h_w of liquid lead was around 348 kW only for the distribution and collection zones. It means that the pump had to at least overcome this energy loss and it should have provided larger power when taking into account the energy losses in other parts of the secondary circuit, especially in the heat exchanger.

3.3. Heat Transfer Analysis

From Figure 10 it can be seen that the molten salt temperature was continuously increasing from the center to the external circumference and the liquid lead had a relative uniform temperature distribution (Figure 13). This can be easily explained by the characteristics of the cross (lower part) and co-current flows (upper part). In the center region, there were two factors enhancing the heat transfer: the long flow path of molten salt crossing the fuel tubes (Figure 14) and the large velocity difference between molten salt and liquid lead. The heat transfer was weak due to the low velocity difference in the peripheral region, which resulted in a high molten salt temperature. Since the radial distribution of power in the core follows a Bessel function of order zero (first period), the heat transfer enhancement in the center region could compensate the power peak and flatten the temperature distribution to achieve a higher operational temperature for both molten salt and liquid lead, which means the potential for a higher power density.

The exchanged heat between molten salt and liquid lead in the distribution zone resulted in their enthalpies changing and yielding a total thermal power transfer of 1.65 MW for this one twelfth sector. Considering the whole structure and including the collection zone, the heat power transferred increased to 39.6 MW, which was around 40% of the total thermal power. It means that the distribution zone as well as the collection zone not only distributed and collected the fluids, but also had a significant impact on the total heat removal process of the core, while the remainder thermal energy was transferred inside the core zone.

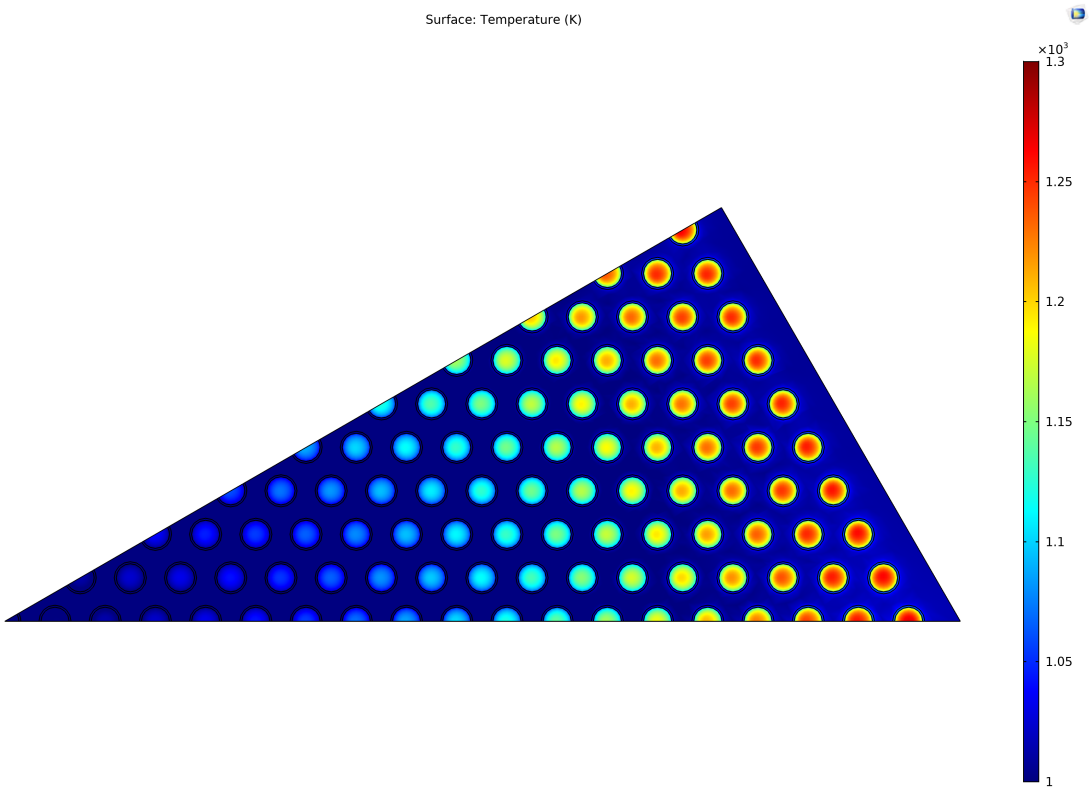

Figure 13. Temperature distribution at the outlet plane.

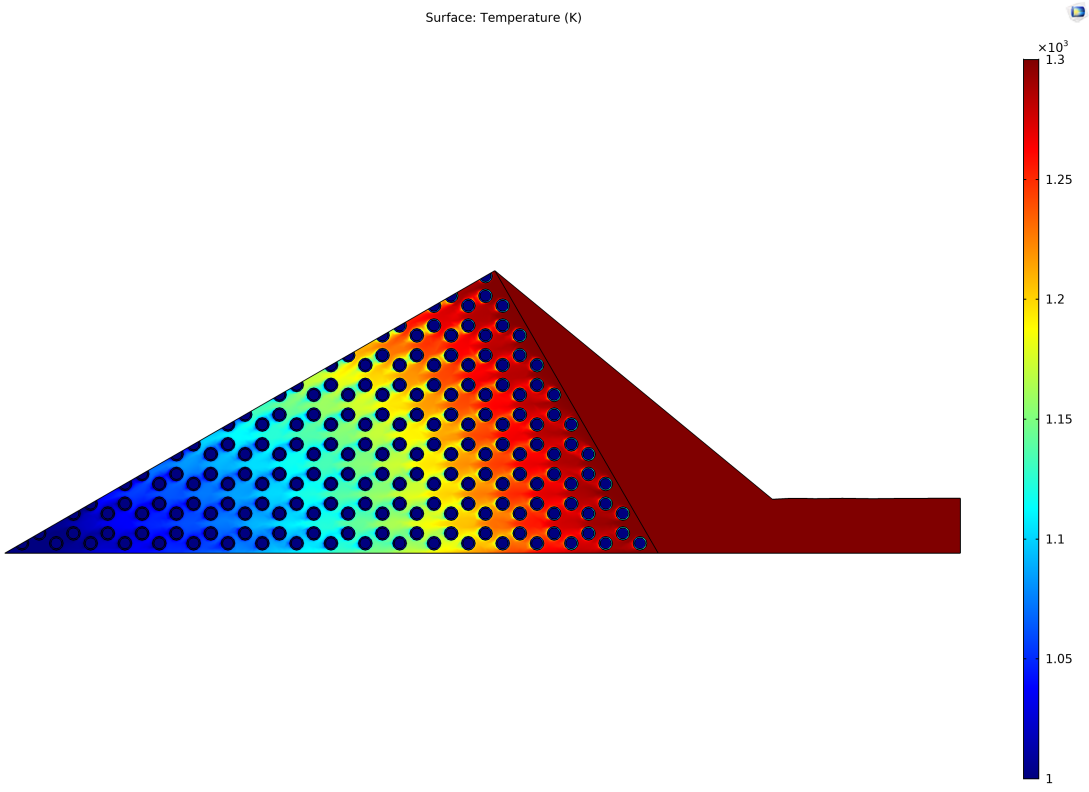

Figure 14. Temperature distribution at the plane of the fuel inlet pipe.

3.4. Sensitivity Analysis of Inlet Velocities

In order to investigate the influence of the inlet velocities on the thermal-hydraulic characteristics of the distribution zone, five inlet scenarios (Table 5: I0 for the original one and I1 to I4 for the changed inlet velocities) were simulated and compared.

Table 4. Mesh Scenarios.

Parameters	M0	M1	M2	M3	M4
Element size	Original	Original	Original	Coarse	Fine
Number of boundary layers	6	3	8	6	6
Number of elements	599,333	502,525	545,028	515,312	825,333
Average element quality	0.6259	0.6179	0.6222	0.596	0.6758
Minimum element quality	4.447×10^{-5}	3.75×10^{-6}	3.686×10^{-6}	3.467×10^{-6}	9.606×10^{-6}

Table 5. Inlet Scenarios.

Parameters	I0	I1	I2	I3	I4
Molten salt inlet velocity (m/s)	3.0	2.5	3.5	3.0	3.0
Liquid lead inlet velocity (m/s)	5.0	5.0	5.0	4.0	6.0

As shown in Figure 15, the magnitude of outlet velocity of molten salt was proportional to its inlet velocity and its profile's shape was similar. The same conclusion can be made for the liquid lead. The temperature profile of liquid lead (Figure 16) was not influenced too much by the inlet velocities thanks to its heat capacity and mass flow rate. However, the thermal behaviour of the molten salt was influenced by its inlet velocity: a higher molten salt inlet velocity resulted in a higher magnitude but a similar trend in the temperature profiles and vice-versa. The impact of the liquid lead's inlet velocity on the molten salt's temperature profile was negligible, which means that the heat transfer between the fluids in the distribution zone occurred mainly in the lower part (cross flow). It has to be pointed out that the heat transfer in the core zone (co-current flow) was definitely influenced by the velocity variation of both fluids due to the change of relative velocity between them, and a strong coupling effect should be considered during transient conditions with rapid velocitiy variation expected. The thermal hydraulic coupling effects between the molten salt and liquid lead, as well as the thermal hydraulics-neutronics coupling, will have to be considered for further simulations of the core, especially in the case of transients and accident situations.

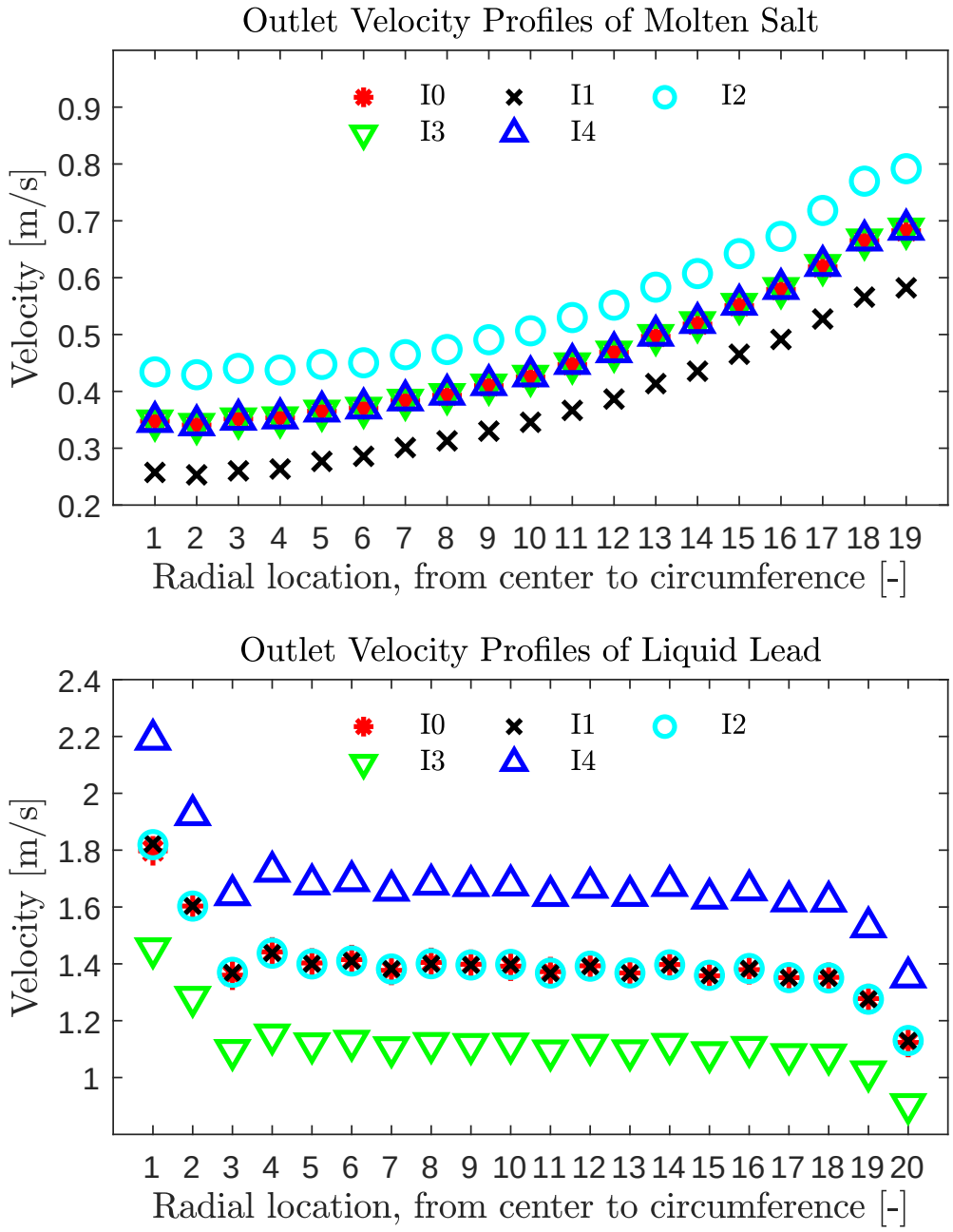

Figure 15. Outlet velocity distribution at various inlet scenarios: top, velocity profiles of molten salt; bottom, velocity profiles of liquid lead.

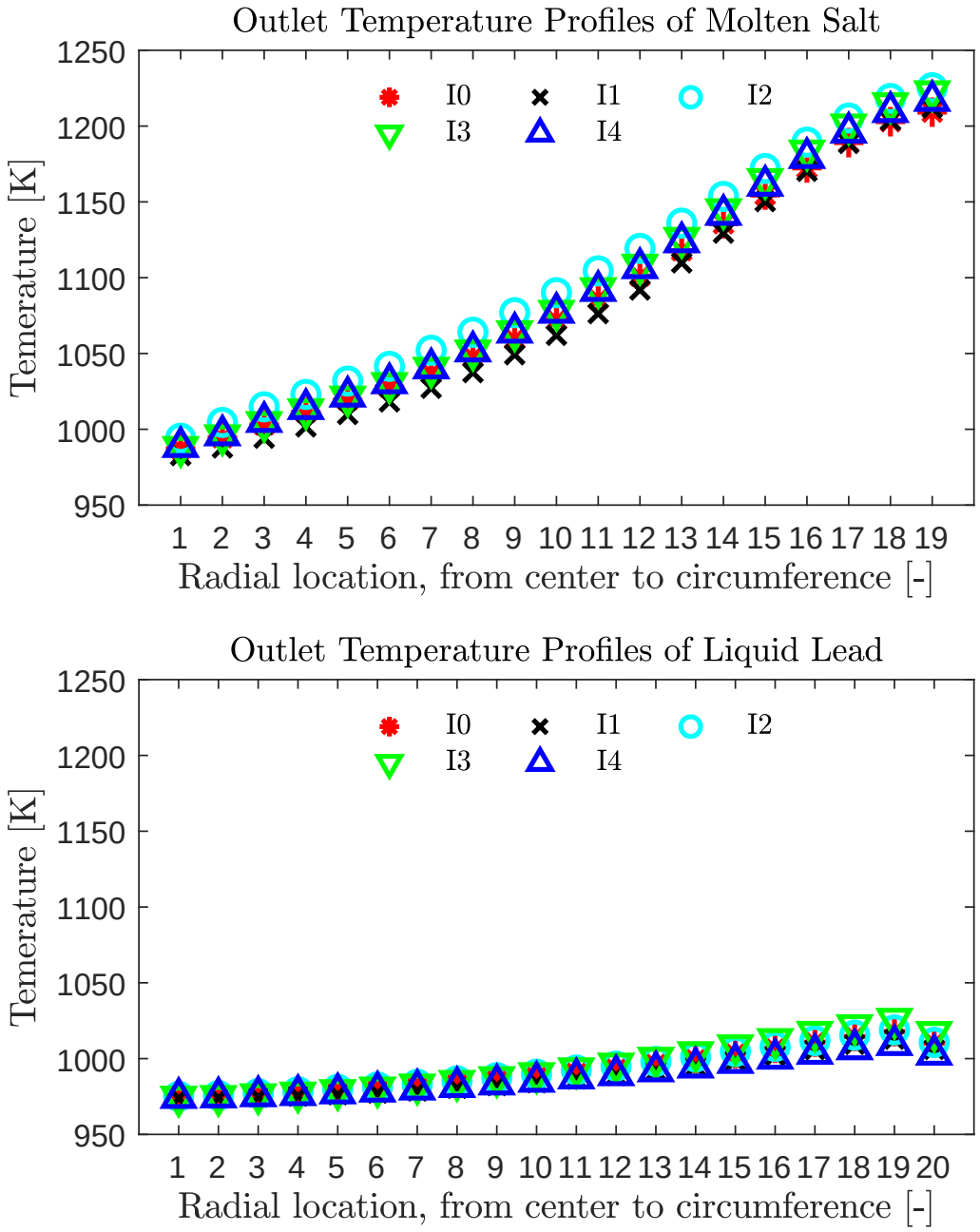

Figure 16. Outlet temperature distribution at various inlet scenarios: top, temperature profiles of molten salt; bottom, temperature profiles of liquid lead.

4. Conclusions

The computer model built by COMSOL Multiphysics is verified by examining the value of the wall resolution in viscous units and by performing mesh sensitivity studies. The energy loss and heat exchange in the distribution zone are quantified, and it is found that the pumping power delivered to the liquid lead has to be much larger than that required by the molten salt in order to overcome the large frictional energy loss of the flowing liquid lead. An amount of thermal power corresponding to about 40% of the total reactor thermal power is transferred in the distribution and collection zones, which not only affects the hydraulic performance of both fluids but also has a significant influence on

the heat removal process. Since the radial distribution of power in the core follows a Bessel function of order zero (first period), the heat transfer enhancement in the center region could compensate the power peak and flatten the temperature distribution to achieve a higher operational temperature for both molten salt and liquid lead, which means the potential for a higher power density. The outlet velocity profiles observed are proportional in magnitude to the inlet velocity ones with a similar shape.

Author Contributions: Conceptualization, C.L. and R.L.; methodology, C.L.; software, C.L. and X.L.; validation, C.L.; formal analysis, C.L.; investigation, C.L.; resources, C.L.; data curation, C.L.; writing—original draft preparation, C.L.; writing—review and editing, C.L. and R.M.-J.; visualization, C.L. and X.L.; supervision, R.M.-J.; project administration, R.M.-J.; funding acquisition, R.M.-J. All authors have read and agreed to the published version of the manuscript.

Funding: This research received no external funding.

Acknowledgments: We would like to thank M. Seidl and X. Wang for their strong support and technical input, to the research group at IFK for providing basic data and very fruitful discussions on the design characteristics of the DFR concept.

Conflicts of Interest: The authors declare no conflict of interest.

Abbreviations

The following abbreviations are used in this manuscript:

SMDFR	Small Modular Dual Fluid Reactor
LBE	Lead-Bismuth Eutectic
CFD	Computational Fluid Dynamics
MSBR	Molten Salt Breeder Reactor
DFR	Dual Fluid Reactor
IFK	Institue for Solid-State Nuclear Physics
FEM	Finite Element Method
RANS	Reynolds-Averaged Navier-Stokes
SI	International System of Units

All the quantities in this work are expressed according to the International System of Units (SI) and to the nomenclature listed here below.

ρ	density	T	absolute temperature
$\mathbf{u}$	average velocity field	$\mathbf{q}$	heat flux by conduction
p, P	pressure	k	heat conductivity
$\mathbf{I}$	identity matrix	$\mathbf{n}$	normal vector
$\mathbf{K}$	viscosity term	u_τ	friction velocity
$\mathbf{F}$	body force vector	T_w	wall temperature
μ	dynamic viscosity	T_f	fluid temperature
μ_T	turbulent viscosity	T_+	dimensionless temperature
k	turbulent kinetic energy	Pr_T	turbulent Prandtl number
ϵ	turbulent dissipation rate	g	gravitational acceleration
$C_{\epsilon 1}$	model constant	z	axial coordinate
$C_{\epsilon 2}$	model constant	u	velocity
C_μ	model constant	A	cross section area
σ_k	model constant	h_w	energy loss
σ_ϵ	model constant	D	diameter
C_p	specific heat at constant pressure	H	height

References

1. Robertson, R.; Briggs, R.; Smith, O.; Bettis, E. *Two-Fluid Molten-Salt Breeder Reactor Design Study (Status as of January 1, 1968)*; Technical Report; Oak Ridge National Lab.: Oak Ridge, TN, USA, 1970.

2. Singh, V.; Lish, M.R.; Wheeler, A.M.; Chvála, O.; Upadhyaya, B.R. Dynamic Modeling and Performance Analysis of a Two-Fluid Molten-Salt Breeder Reactor System. *Nucl. Technol.* **2018**, *202*, 15–38, doi:10.1080/00295450.2017.1416879. [CrossRef]
3. Taube, M.; Ligou, J. Molten plutonium chlorides fast breeder reactor cooled by molten uranium chloride. *Ann. Nucl. Sci. Eng.* **1974**, *1*, 277–281. [CrossRef]
4. Huke, A.; Ruprecht, G.; Weißbach, D.; Gottlieb, S.; Hussein, A.; Czerski, K. The Dual Fluid Reactor–A novel concept for a fast nuclear reactor of high efficiency. *Ann. Nucl. Energy* **2015**, *80*, 225–235. [CrossRef]
5. Wang, X.; Macian-Juan, R.; Seidl, M. Preliminary analysis of basic reactor physics of the Dual Fluid Reactor-15270. In Proceedings of the ICAPP 2015, Nice, France, 3–6 May 2015.
6. Wang, X. Analysis and evaluation of the dual fluid reactor concept. Ph.D. Thesis, Universitätsbibliothek der TU München, Munich, Germany, 2017.
7. Wang, X.; Macian-Juan, R. Comparative Study of Basic Reactor Physics of the DFR Concept Using U-Pu and TRU Fuel Salts. In Proceedings of the International Conference on Nuclear Engineering. American Society of Mechanical Engineers, Shanghai, China, July 2-6, 2017; Volume 57830, p. V005T05A001.
8. Wang, X.; Macian-Juan, R. Comparative Study of Thermal-Hydraulic Behavior of the DFR Using U-Pu and TRU Salt Fuels. In Proceedings of the International Conference on Nuclear Engineering. American Society of Mechanical Engineers, Shanghai, China, July 2-6, 2017; Volume 57847, p. V006T08A004.
9. Wang, X.; Macian-Juan, R. Steady-state reactor physics of the dual fluid reactor concept. *Int. J. Energy Res.* **2018**, *42*, 4313–4334. [CrossRef]
10. Wang, X.; Liu, C.; Macian-Juan, R. Preliminary hydraulic analysis of the distribution zone in the Dual Fluid Reactor concept. *Prog. Nucl. Energy* **2019**, *110*, 364–373. [CrossRef]
11. IAEA. Nuclear Desalination. Available online: https://www.iaea.org/topics/non-electric-applications/nuclear-desalination. (accessed on 30 July 2020).
12. Desyatnik, V.; Katyshev, S.; Raspopin, S.; Chervinskii, Y.F. Density, surface tension, and viscosity of uranium trichloride-sodium chloride melts. *Sov. At. Energy* **1975**, *39*, 649–651. [CrossRef]
13. Nilsson, O.; Mehling, H.; Horn, R.; Fricke, J.; Hofmann, R.; Mueller, S.; Eckstein, R.; Hofmann, D. Determination of the thermal diffusivity and conductivity of monocrystalline silicon carbide (300-2300 K). *High Temp. High Press.* **1997**, *29*, 73. doi:10.1068/htec142. [CrossRef]
14. Fazio, C.; Sobolev, V.; Aerts, A.; Gavrilov, S.; Lambrinou, K.; Schuurmans, P.; Gessi, A.; Agostini, P.; Ciampichetti, A.; Martinelli, L.; et al. *Handbook on Lead-Bismuth Eutectic Alloy and Lead Properties, Materials Compatibility, Thermal-Hydraulics and Technologies*, 2015 ed.; Technical Report; Organisation for Economic Co-Operation and Development: Paris, France, 2015.
15. Huke, A.; Ruprecht, G.; Weißbach, D.; Czerski, K.; Gottlieb, S.; Hussein, A.; Herrmann, F. Dual-fluid reactor. In *Molten Salt Reactors and Thorium Energy*; Elsevier: Amsterdam, The Netherlands, 2017; pp. 619–633.
16. *Introduction to COMSOL Multiphysics*; COMSOL: Stockholm, Schweden, 2019.
17. *CFD Module User's Guide*; COMSOL: Stockholm, Schweden, 2019.
18. *Heat Transfer Module User's Guide*; COMSOL: Stockholm, Schweden, 2019.
19. Carasi, B. Compressibility Options and Buoyancy Forces for Flow Simulations. 2016. Available online: https://www.comsol.com/blogs/compressibility-options-and-buoyancy-forces-for-flow-simulations (accessed on 30 July 2020).
20. Griesmer, A. Size Parameters for Free Tetrahedral Meshing in COMSOL Multiphysics. 2014. Available online: https://www.comsol.com/blogs/size-parameters-free-tetrahedral-meshing-comsol-multiphysics (accessed on 30 July 2020).